Orbital angular momentum in the near-field of a fork grating

Author(s):
Dettlaff, Krispin M.; Mavrona, Elena; Zolliker, Peter; Hack, Erwin

Publication date:
2023-05-08

Permanent link:
https://doi.org/10.3929/ethz-b-000614375

Originally published in:
Optics Express 31(10), https://doi.org/10.1364/OE.486143

Research Article Vol. 31, No. 10 / 8 May 2023 / Optics Express 15757
Optics EXPRESS

Orbital angular momentum in the near-field of a fork grating

KRISPIN M. DETTLAFF,[1,2] ELENA MAVRONA,[1] PETER ZOLLIKER,[1] AND ERWIN HACK[1,*]

[1]Transport at Nanoscale Interfaces Laboratory, Empa, Uberlandstrasse 129, Dubendorf, CH-8600, Switzerland
[2]Optical Materials Engineering Laboratory, ETH Zurich, Leonhardstrasse 21, Zürich, CH-8092, Switzerland
*erwin.hack@empa.ch

Abstract: Light beams with Orbital Angular Momentum (OAM) are explored in applications from microscopy to quantum communication, while the Talbot effect revives in applications from atomic systems to x-ray phase contrast interferometry. We evidence the topological charge of an OAM carrying THz beam in the near-field of a binary amplitude fork-grating by means of the Talbot effect, which we show to persist over several fundamental Talbot lengths. We measure and analyze the evolution of the diffracted beam behind the fork grating in Fourier domain to recover the typical donut-shaped power distribution, and we compare experimental data to simulations. We isolate the inherent phase vortex using the Fourier phase retrieval method. To complement the analysis, we assess the OAM diffraction orders of a fork grating in the far-field using a cylindrical lens.

1. Introduction

When Orbital Angular Momentum (OAM) of light entered the scene of optics in the 1990s, it raised many expectations [1,2] due to its contribution to the total angular momentum, next to the spin angular momentum. While the spin angular momentum is related to the circular polarization of light, light that carries OAM exhibits a helical phase front, from which the terms "twisted light" or "vortex beam" were coined. This phase front includes an azimuthal phase with an integer number l of 2π phase jumps in one round-trip, where l is the topological charge (TC) and its sign corresponds to the azimuthal direction in which the phase is increasing [3]. Consequently, all vortex beams have a phase singularity in their center and show a characteristic donut-shaped intensity distribution.

While OAM offers an additional degree of freedom for optical communication [4], it is exploited in many other fields like high-resolution microscopy [5], nanostructure fabrication [6] optical tweezers [7], or quantum key distribution [8]. To generate the helical phase front, laser cavity tuning [9] and interference methods [10] have been reported, but also specially designed phase elements including spiral phase plates [11,12], zone plates [13], lenses [14], spatial light modulators [15] and fork gratings [16]. Fork gratings have become popular because they are readily available for all spectral ranges, while the generated vortex beams are of high quality, which is crucial for real-world applications. In this paper, we work in the THz regime. THz beams are non-ionizing and penetrate many materials like synthetics and natural substances [17]. Progress can be expected in applying non-conventional laser beams, e.g. OAM carrying Airy beams, in this spectral range [18].

The far-field diffraction of a binary fork grating shows a fan of well separated OAM carrying beamlets with different TC in each diffraction order. The characteristic donut-shaped intensity

#486143 https://doi.org/10.1364/OE.486143
Journal © 2023 Received 19 Jan 2023; revised 27 Mar 2023; accepted 27 Mar 2023; published 26 Apr 2023

Optics EXPRESS

distribution and its corresponding vortex phase distribution are readily measured in the far-field by lens imaging [19], interferometry [20–22] or phase-shifting holography [23]. To analyze the OAM spectrum of a propagating beam, phase-stepping interferometry with a Gaussian beam was reported [24]. Recently, the TC of an incoming vortex beam has been measured using the Talbot effect of a regular grating [25]. Here, however, we generate a OAM beam with a fork grating and analyze the TC directly in its near-field. In the near-field, all diffraction orders overlap and several topological charges are simultaneously present.

As the fork grating has also a (quasi) periodic structure, a (pseudo) Talbot effect is expected in the near-field. When illuminating a periodic diffractive optical element (DOE) with monochromatic radiation of wavelength λ, the Talbot effect [26] becomes manifest in the self-imaging of the grating on parallel planes separated by the so-called fundamental Talbot length $L_T = 2p^2/\lambda$ and its multiples, where p is the grid constant of the grating. Self-imaging is exploited in many applications: Talbot-Lau interferometry is used to show matter waves [27] and interaction effects of atoms in a periodic potential [28], and it enables X-Ray phase-contrast imaging in medical applications [29]. The self-images with higher harmonics of the DOE allow focusing light to a subwavelength scale, which benefits laser lithography [30]. The Talbot effect has been explored in cases that include ring-shaped [31], radial and azimuthal periodicities [32], Siemens stars [33], generalized 2D-gratings [34] and for non-paraxial situations [35,36].

While the vortex beam carries OAM from the moment that it passes through the fork grating, a method to evidence OAM in the near-field diffraction field right after its production has not been reported, to the best of our knowledge. We propose here a method to evidence OAM from fork gratings in the near-field using the Talbot effect and Fourier analysis. Single and double bifurcation gratings are analyzed. While we work in the THz regime, the method is readily applicable to other wavelength ranges.

2. Theory

A binary amplitude fork grating is a disturbed one-dimensional amplitude grating, in which one or several bifurcations form a fork-like structure. The number of bifurcations or, equivalently, the difference of the number of grating lines below and above the fork determines the magnitude l of the TC. Figure 1(a) shows a fork grating with a single bifurcation, represented by its first order phase distribution. This pattern can be seen as the superposition of a tilted plane wave, Fig. 1(b), with a helical wave, Fig. 1(c), shown as a vortex phase distribution in first order. It can also be regarded as a carrier wave, Fig. 1(b), with an information-bearing wave, Fig. 1(c), resulting in the modulated signal, Fig. 1(a). The grating period p is the inverse of the spatial carrier frequency in Fig. 1(b) used to modulate the vortex signal. In this context, Fig. 1 shows a transmission protocol, namely the encoding of a message as a TC. Therefore, a decoding process in the form of a demodulation would allow the receiver to read the TC of the fork.

Let the grating plane be described by the coordinate system $\mathbf{r} = (x, y)$ so that the y-axis is parallel to the grating lines of the carrier. Further, we introduce the cylindrical coordinates $\phi = \arctan(x, y)$, $r = \sqrt{x^2 + y^2}$ and z, the propagation direction of the incoming wave. The amplitude transmittance function T of the fork grating is represented by the Fourier series:

$$T(\mathbf{r}) = \sum_{n=-\infty}^{\infty} T_n \exp\left[in\left(\frac{2\pi}{p}x + l\phi\right)\right]. \tag{1}$$

Let the incident plane wave have the complex amplitude distribution $u_0(\mathbf{r})$ at the grating plane. Immediately after the grating, the complex amplitude distribution acquires the form:

$$\psi(x, y, z = 0) = u_0(\mathbf{r}) \times T(\mathbf{r}) = \sum_{n=-\infty}^{\infty} T_n\, u_0(\mathbf{r}) \exp\left[in\left(\frac{2\pi}{p}x + l\phi\right)\right]. \tag{2}$$

Optics EXPRESS

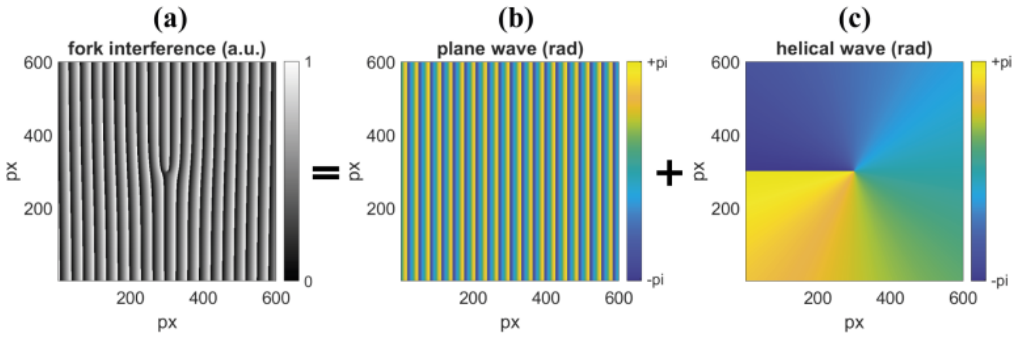

Fig. 1. Phase distribution. A fork grating with a single bifurcation (a) is the superposition of a plane wave (b) with a helical wave (c).

Equation (2) implies that the grating period p of the carrier introduces a linear phase in x-direction to the incoming beam, while the second phase term $l\phi$ leads to a continuous change of the grating period. We express the evolution of the wave function in z-direction using direction cosines [37],

$$\psi(x,y,z) = \int_{-\infty}^{\infty}\int_{-\infty}^{\infty} A\left(\frac{\alpha}{\lambda},\frac{\beta}{\lambda},0\right)\exp\left(i\frac{2\pi}{\lambda}\sqrt{1-\alpha^2-\beta^2}z\right)\times\exp\left[i2\pi\left(\frac{\alpha}{\lambda}x+\frac{\beta}{\lambda}y\right)\right]d\frac{\alpha}{\lambda}d\frac{\beta}{\lambda}, \tag{3}$$

where

$$A\left(\frac{\alpha}{\lambda},\frac{\beta}{\lambda},0\right) = \int_{-\infty}^{\infty}\int_{-\infty}^{\infty}\psi(x,y,0)\exp\left[-i2\pi\left(\frac{\alpha}{\lambda}x+\frac{\beta}{\lambda}y\right)\right]dxdy \tag{4}$$

are the Fourier components of the field distribution right after the grating. Equation (4) describes the angular spectrum when considering $k_x = \alpha k$ and $k_y = \beta k$, respectively. The direction cosines α, β, γ that describe the propagating wave vector $\boldsymbol{k}$ are interrelated through:

$$\gamma = \sqrt{1-\alpha^2-\beta^2}. \tag{5}$$

Note that for $\alpha^2+\beta^2 > 1$, γ becomes complex and describes the rapidly attenuated evanescent waves. The diffraction integral has been solved analytically in the Fresnel and Fraunhofer regimes for an incoming Gaussian beam to derive the donut shape of the diffraction orders [38]. Assuming a plane wave with constant amplitude across the grating, $u_0(\mathbf{r}) = 1$, the Fourier components of the field distribution are dominated by the grating, Eq. (1), and are

$$\begin{aligned} A\left(\tfrac{\alpha}{\lambda},\tfrac{\beta}{\lambda},0\right) &= \sum_{n=-\infty}^{\infty} T_n \int_{-\infty}^{\infty}\int_{-\infty}^{\infty}\exp\left[in\left(\tfrac{2\pi}{p}x+l\phi\right)-i2\pi\left(\tfrac{\alpha}{\lambda}x+\tfrac{\beta}{\lambda}y\right)\right]dxdy \\ &= 4\pi^2\sum_{n=-\infty}^{\infty} T_n\delta\left[\left(\tfrac{n}{p}-\tfrac{\alpha}{\lambda}\right)\right]\delta\left[\tfrac{\beta}{\lambda}\right] \qquad \text{for } l=0. \end{aligned} \tag{6}$$

Inserting into Eq. (3) yields

$$\psi(x,y,z) = 4\pi^2\sum_{n=-\infty}^{\infty} T_n\exp\left(i\,2\pi\sqrt{\frac{1}{\lambda^2}-\frac{n^2}{p^2}}z\right)\times\exp\left[i2\pi\left(\frac{n}{p}x\right)\right]. \tag{7}$$

This field distribution is proportional to that of the original diffraction plane, Eq.(2), at distances for which

$$\exp\left(i\,2\pi\sqrt{\frac{1}{\lambda^2}-\frac{n^2}{p^2}}z\right) = \exp\left(i\,2\pi\frac{z}{\lambda}\right) \tag{8}$$

Optics EXPRESS

where the constant phase factor on the r.h.s. is the free space propagation. This yields the well-known Talbot distance [39]

$$L_T = \frac{\lambda}{1 - \sqrt{1 - \frac{n^2\lambda^2}{p^2}}} \approx \frac{2p^2}{n^2\lambda}. \tag{9}$$

The Talbot effect repeats the field distribution, and hence the phase, of the DOE in multiples of the fundamental Talbot length at $z = q\,L_T$, where $q \in \mathbb{N}$. Note that as Eq. (9) holds for $n = 1 = q$, it is fulfilled for all orders with $q = n^2$.

While the derivation of Eq. (9) strictly holds only for $l = 0$, we expect a pseudo Talbot effect for a fork grating. Here, the line density changes from $p = S/N$ to $S/(N + l)$ from the bottom to the top of the grating, where S is the width of the grating and N the number of the illuminated lines, which leads to a reduction of the Talbot length. In other words, the TC l must be much smaller than the number N of illuminated lines for the Talbot effect to be observable.

In order to assess the self-imaging, we simulated the near-field diffraction using the angular spectral method of Eq. (3) [37]. Self-imaging in real space is reflected by self-imaging in Fourier space, in that the Fourier transform at the Talbot plane matches the Fourier transform of the grating plane, given by Eq. (2). We have shown earlier that the self-imaging can be identified using the normalized Pearson correlation coefficient (PCC) applied to the stack of Fourier spectra [34]:

$$R = \frac{\sum_0^m \sum_0^n (A_{mn} - \bar{A})(B_{mn} - \bar{B})}{\sqrt{\left(\sum_0^m \sum_0^n (A_{mn} - \bar{A})^2\right)\left(\sum_0^m \sum_0^n (B_{mn} - \bar{B})^2\right)}}. \tag{10}$$

where A_{mn} and B_{mn} are the values at row m and column n in the discrete power spectrum A and B, respectively, and $\bar{A}$ and $\bar{B}$ are the averages of A and B. The summation is limited to the most significant frequency range comprising the fundamental frequency and optionally some higher harmonics. The PCC is calculated for each pair from the full stack of Fourier spectra.

It is well known that the far-field diffraction pattern corresponds to the Fourier transform of the diffraction plane, which in turn also corresponds to the Fourier transform at the Talbot planes. Similarly, the Fourier spectrum of a binary fork grating represents the field distribution of the far-field. The spatial carrier frequency corresponds to the first diffraction order in the far-field. This allows to identify both the ring shape and the phase vortex in the near-field. We find the wrapped phase vortex of the grating by using the Fourier Transform method of phase retrieval [40], which is performed by band-pass filtering the region around the carrier frequency, followed by the inverse Fourier transform. According to Eq. (2), the two-dimensional intensity distribution of the self-image in first order is:

$$\begin{aligned} I(x,y) = |\psi(x,y)|^2 &= |u_0(\mathbf{r})|^2 \left| T_0 + T_1 \exp\left[i\left(\tfrac{2\pi}{p}x + l\phi\right)\right] + T_{-1} \exp\left[-i\left(\tfrac{2\pi}{p}x + l\phi\right)\right]\right|^2 \\ &= I_b(x,y) + I_m(x,y)\exp[i(2\pi f_c x + l\phi)] + I_m(x,y)\exp[-i(2\pi f_c x + l\phi)] + h.h. \end{aligned} \tag{11}$$

Here, I_b, I_m and ϕ are the background intensity, the modulation intensity and the phase to be determined, respectively, while h.h. are higher harmonics and $f_c = p^{-1}$ is the carrier frequency. The Fourier spectrum of the intensity distribution of Eq. (11) is:

$$\mathrm{I}(f_x, f_y) = \mathrm{I}_b(f_x, f_y) + C(f_x - f_c, f_y) + C*(f_x + f_c, f_y). \tag{12}$$

Here, the capital calligraphy letters indicate the Fourier transform of their italic lowercase counterparts and (f_x, f_y) are the frequency coordinates corresponding to (x,y). If f_c is large enough, the spectra of $I_b(f_x, f_y)$, $C(f_x, f_y)$, and $C^*(f_x, f_y)$ are separated in the frequency domain. The

Optics EXPRESS

component $C(f_x - f_c, f_y)$ can be isolated by band-pass filtering. A subsequent inverse Fourier transform yields the complex field distribution $c(\boldsymbol{x})$. Finally, the wrapped phase is retrieved from

$$\phi(\boldsymbol{x}) = \arctan 2 \left\{ \frac{\mathrm{Im}[c(\boldsymbol{x})]}{\mathrm{Re}[c(\boldsymbol{x})]} \right\}. \tag{13}$$

3. Experiment

The experiments were performed on Ronchi fork gratings with single and double bifurcation. The design was computer generated; the fabrication was done by wafer processing techniques including spin coating, laser writing, reactive ion etching and lift-off. The gold structures were fabricated on top of a cyclic olefin copolymer (TOPAS COC) film, which is transparent for THz radiation [41]. Figure 2(a) shows a photograph of the DOE with a double-bifurcation, see close-up in Fig. 2(b). This singularity is the origin of the two additional grating lines on the upper half of the grating.

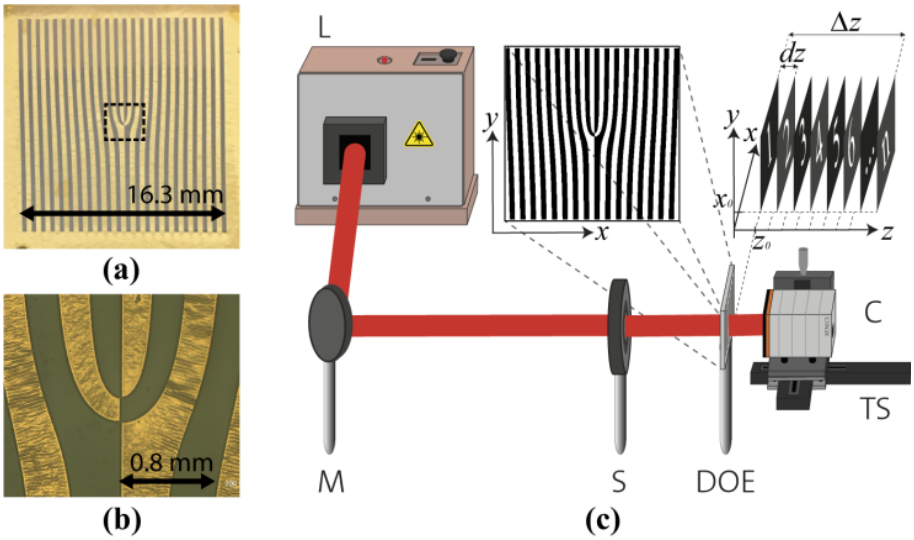

Fig. 2. Experimental setup for near-field measurements. (a) Photo of a double-bifurcation fork grating (Ronchi). (b) Microscopic image taken from the black-dashed rectangle in (a). (c) Experimental setup for the near-field diffraction measurement. The beam of the THz gas-laser [L] was directed via a mirror [M] through a diaphragm shutter [S] and the DOE to the camera [C]. The translation stage [TS] moved the camera in z-direction in steps of dz over a range of Δz.

The experimental setup for the near-field diffraction experiments is depicted in Fig. 2(c). It consists of a CH_3OH THz gas laser (FIRL 100 system, Edinburgh Instruments, Livingstone, UK), a DOE (fork grating) and an uncooled microbolometer camera (Gobi-640-GigE, Xenics, Leuven, BE). To create an image stack in the near-field, the camera was moved on a motorized translation stage (MTS50-Z8, Thorlabs, Newton, USA) in z-direction over a range of $\Delta z > 16$ mm starting at near contact of the DOE with the camera window. The smallest gap between camera sensor and DOE of roughly 6 mm was considered in the analysis. Every $dz = 50\,\mu$m an image was taken. A diaphragm shutter (SHB1T, Thorlabs, Newton, USA) was used for infrared background subtraction. For the experiment with the single-bifurcation fork grating a second translation stage of the same type was used to move the camera in x-direction. Additional images every $dx = 5$ mm were stitched together to obtain a synthetic aperture for each z-position.

Optics EXPRESS

Far-field experiments of the beam shape were done with the aid of a plano-convex lens (PTL-1.5"-100mm-AS, Microtech Instruments, Eugene, USA) placed between DOE and camera to reduce the size of the individual diffraction orders for imaging. Further, a cylindrical lens (CL) with a focal length of 120 mm was 3D-printed in-house from TOPAS and was placed between the DOE and the camera to confirm the topological charge in the far field [42]. The evaluation of the data as well as the simulations were performed using MATLAB. To obtain representative results, the pixel resolution of the simulated fork-gratings was made in sufficient resolution to be processed on a usual workstation (single bifurcation grating: 1033×947 px; double bifurcation grating: 981×988 px). Further, attention was paid that the fork grating holograms covered the same area as those produced in the gold structures, e.g. Figure 2(a). The near-field diffraction was generated using the angular spectrum method and was cut out corresponding to the pixel resolution of the bolometer camera, considering the synthetic aperture acquisition and zero-padding.

4. Results and discussion

4.1. Single bifurcation grating

The single-bifurcation fork grating with an opening ratio of 0.5 (Ronchi) was tested for self-imaging. The pitch of the fork grating varied from $p_{bottom} \cong 800\,\mu m$ to $p_{top} \cong 780\,\mu m$, with an increased variation close to the singularity in the center. Considering the laser wavelength of 118.8 µm, Eq. (9) predicts the fundamental Talbot length at $L_T = 5.12$ mm and 5.39 mm for top and bottom, respectively.

The image stack for the single-bifurcation experiment covered a range of $\Delta z = 17$ mm. To avoid the interference of the grating lines with the pixel matrix, the sample was rotated by 45°. Further, synthetic aperture acquisition was applied to increase the image area. Figure 3(a) and Fig. 3(d) show a stitched and rotated image at $z = 5.9$ mm from the measured and simulated image stack, respectively. The blue background corresponds to the zero-padding applied to increase the frequency resolution.

Because a direct evaluation of the experimental diffraction pattern in the spatial domain was challenging due to slight misalignment, intensity variations and parasitic interference, a Fourier transformation of the data was performed. The power spectra are displayed in Fig. 3(b) and Fig. 3(e) for the experiment and simulation, respectively. The characteristic pattern of a diffraction grating appears. Symmetric orders lying on the $\nu = 0\,mm^{-1}$ frequency axis clearly show up and correspond to the fundamental carrier frequency expected around $1.26\,mm^{-1}$ and its higher harmonics. As the Fourier transform of the grating corresponds to the far-field diffraction orders, we determine the TC from the 1st order, see the orange boxes in Fig. 3(b) and Fig. 3(e), and the respective close-up in Fig. 3(c) and Fig. 3(f). They exhibit ring structures with low intensity centers, as is expected for a vortex beam. The elliptical shape and its orientation of the main axis is a consequence of the camera cutout. Due to experimental effects like illumination variation and a slightly tilted DOE the ellipse in Fig. 3(c) is not completely closed like the one from the simulated data, Fig. 3(f).

The evolution of the 1st order of the Fourier transform over the z-stack is illustrated in Fig. 4(a) and Fig. 4(b) for the experimental and simulated data, respectively. Figure 4 indicates that the self-images of the (spectrum of the) fork grating appear in the Talbot planes at 5.90, 10.65 and 16.15 mm, in agreement with the fundamental Talbot length L_T. The repetitive appearance of the ring structure can be seen more clearly when traveling through the Talbot distance in the stack, see Visualization 1 and Visualization 2 in the SI for the experimental and simulated data, respectively. The beam evolution gives insight in the Talbot effect and its fundamental Talbot length L_T.

For an improved quantitative assessment of the self-imaging, the PCC, Eq. (10), was calculated for the 1st order area of the Fourier spectra. The resulting PCC maps from experimental, Fig. 5(a),

Optics EXPRESS

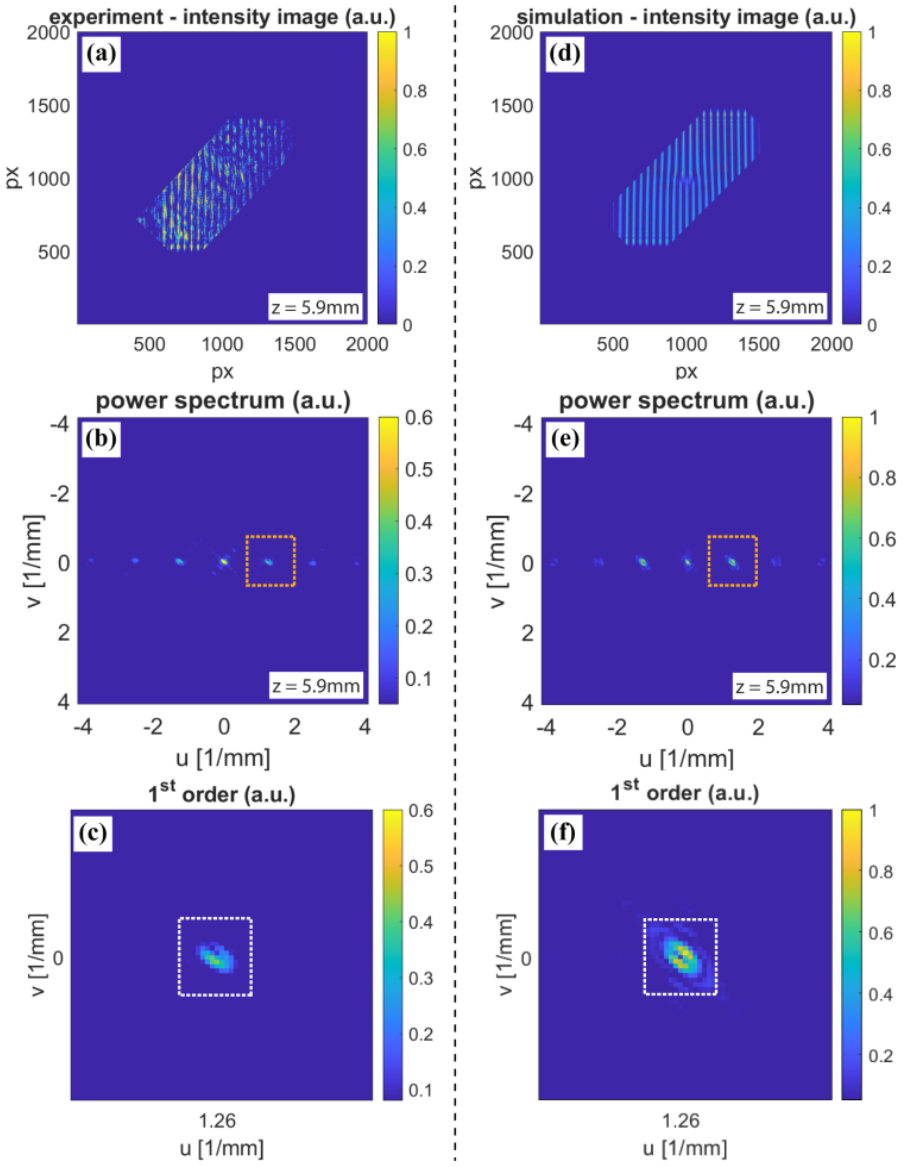

Fig. 3. Fourier analysis of a single bifurcation grating. Intensity images at $z = 5.90$ mm behind the DOE from experiment (a) and simulation (d), rotated by 45° with zero padding. (b) and (e) are power spectra of (a) and (d), respectively. The orange dashed rectangle marks the positive 1st order. (c) and (f) are cut-outs of the 1st order in (b) and (e), respectively. The white dashed area delineates the frequency band used for the calculation of the PCC map in Fig. 5.

Optics EXPRESS

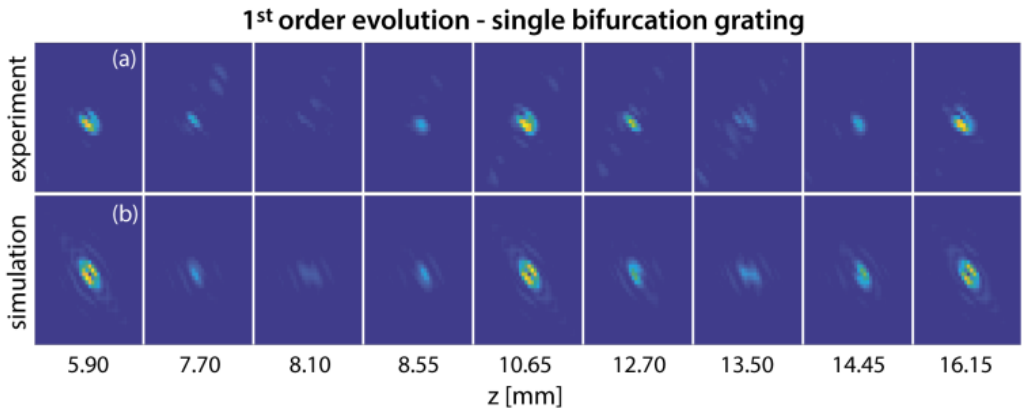

Fig. 4. 1st order beam evolution at some exemplary distances behind the single bifurcation grating from the experimental (a) and simulated (b) data. At regular distances from the fork grating, the Talbot effect appears.

and simulated spectra, Fig. 5(c), are in good agreement. The Talbot effect is visualized by the dark-red lines of high correlation values running across the map parallel to the autocorrelation diagonal line starting at the bottom left. These self-image ridges are not straight as highlighted by the white-dashed lines. The non-linearity of these self-imaging lines is a consequence of the TC.

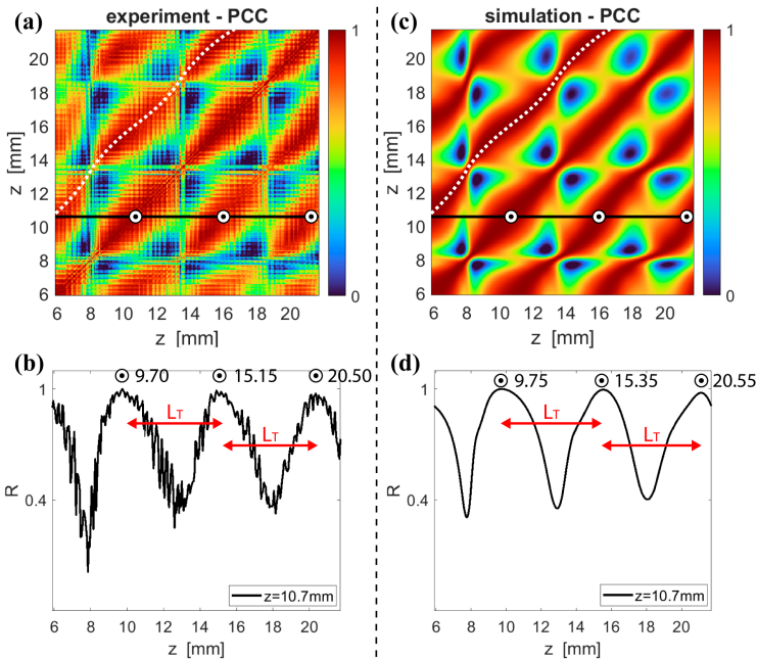

Fig. 5. PCC maps generated from the first order Fourier component from experiment (a) and simulation (c). Both maps show self-imaging (highlighted by white dashed lines). (b) and (d) are cross-sections taken along the black line in (a) and (c), respectively. The black rings mark the maxima of the curves which are separated by the fundamental Talbot length L_T (red arrows).

Optics EXPRESS

The horizontal black lines taken through the PCC maps represent the PCC values of the Fourier spectrum around the 1st order taken at $z = 10.65$ mm with the entire stack of spectra from 6 to 22 mm. Figure 5(b) and Fig. 5(d) show that the recurrence of the pattern occurs over the full stack. It allows evaluating the fundamental Talbot length L_T from the correlation maxima (black circles) and results in 5.45 mm and 5.35 mm in the experiment, and 5.60 mm and 5.20 mm in the simulation.

Based on the self-imaging effect of the DOE the Fourier spectra allow a phase reconstruction. The Fourier Transform phase retrieval method is applied to the spectrum at $z = 5.90$ mm. Figure 6(a) shows the retrieved wrapped phase from the experimental data. Phase retrieval from the simulated data yields an identical result so its display is waived here. A single bifurcation is clearly visible in the central part of the wrapped phase map. The bifurcation in combination with the ring structure of the 1st order in the power spectrum, Fig. 3(c), is proof of the presence of the TC $|l| = 1$ in the near-field. To demodulate the inherent phase vortex, the carrier frequency was subtracted from the wrapped phase map and the resulting phase vortex with $|l| = 1$ is shown in Fig. 6(b). The helical phase front of the vortex going from $-\pi$ to $+\pi$ is marked by black arrows. Both maps are given in a diamond shape, which corresponds to the measurement area shown in Fig. 3(a).

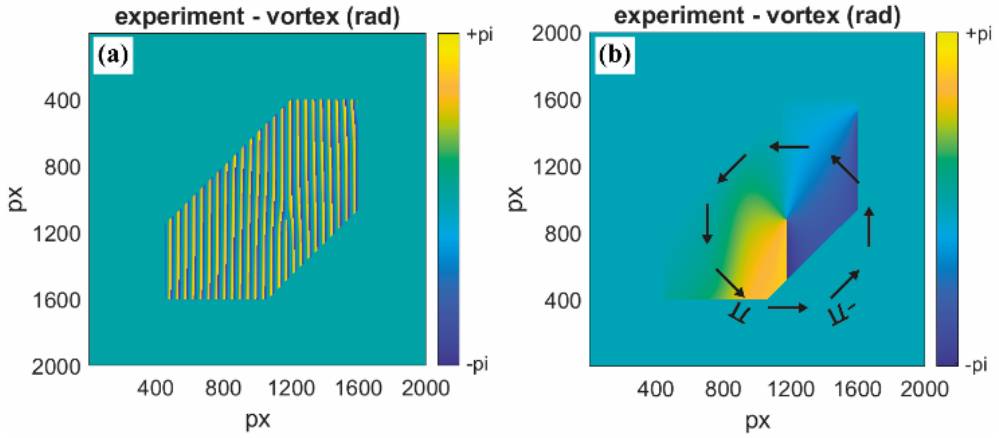

Fig. 6. (a) Retrieved wrapped phase map from the experimental data taken at $z = 5.90$ mm. (b) The corresponding helical phase map after subtraction of a linear phase map corresponding to the carrier frequency. The black arrows indicate the azimuthal phase gradient around the singularity in the center.

4.2. *Double bifurcation grating*

The same procedure was applied to a fork grating with double-bifurcation as shown in Fig. 2(a) and Fig. 2(b). The horizontal pitch in this fork grating varied from $p_{\text{bottom}} \cong 725\,\mu\text{m}$ to $p_{\text{top}} \cong 695\,\mu\text{m}$, corresponding to Talbot distances of 4.42 mm to 4.07 mm, respectively, according to Eq. (9). The stack of near-field images was taken over a range of $\Delta z = 16$ mm. The detector plane and the DOE were aligned parallel in this experiment to get the sharpest self-images. However, this caused a parasitic interference that amplified or reduced the signal during the z-scan.

Figure 7(a) shows the measured intensity distribution at $z = 8.25$ mm, where the self-image had the highest contrast from all images of the stack. This corresponds to the second Talbot plane. Thus, the corresponding power spectrum depicted in Fig. 7(b) reveals a ring like structure in the 1st order (orange dashed rectangle). To increase the frequency resolution the spatial domains were expanded to a size of 2500×2500 pixels with zero padding. The simulation shows

Optics EXPRESS

the corresponding intensity image, Fig. 7(d), and power spectrum, Fig. 7(e). The simulated power spectrum shows a clear ring structure in the 1st order (orange dashed rectangle). Double-bifurcation fork gratings show a larger ring diameter than single-bifurcation ones, compare to Fig. 3(c). The cutout around the 1st order in Fig. 7(c) and Fig. 7(f) reveal that the large ring consists of two partially overlapping rings. The two neighboring minima are an indicator of a vortex beam with twofold topological charge.

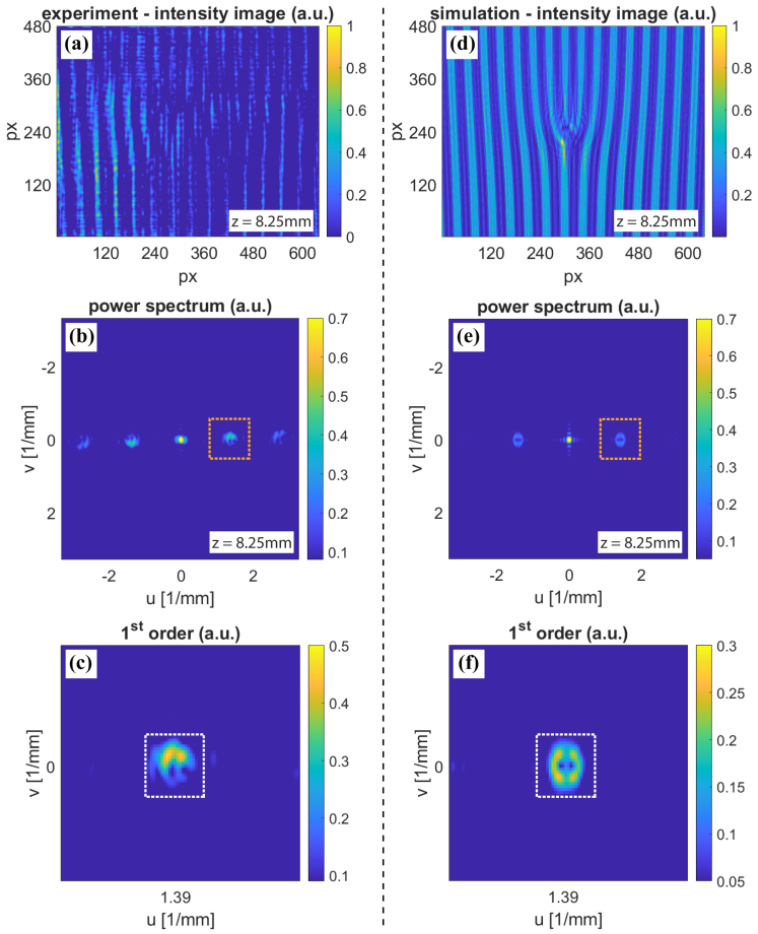

Fig. 7. Fourier analysis of a double bifurcation grating. Intensity images at z = 8.25 mm behind the DOE from experiment (a) and simulation (d). (b) and (e): Power spectra of (a) and (d), respectively. The orange dashed rectangle encloses the positive 1st order. (c) and (f): Cut-out of the positive 1st order calculated with a higher frequency resolution.

The recurrence of the self-imaging distance is less clear from the experimental data. However, the recurrence of the ring structure in the 1st order can be seen more clearly when traveling through the simulated data, see Visualization 3 in the SI. For the sake of completeness, a video generated from the stack of experimental data is available too, see Visualization 4 in the SI, even if the self-imaging is much harder to recognize.

To verify the fundamental Talbot length, a PCC map was generated from the areas marked by the white dashed rectangle in Fig. 7(c) and Fig. 7(f), through the entire stack of power spectra. Figure 8 compares the PCC maps from the spectra of the experimental and simulated data. The parasitic interference induced by the parallel configuration of the detector and DOE-plane

Optics EXPRESS

contributed a strong ripple structure in the experimental data, see Fig. 8(a) and Fig. 8(b). In contrast, the PCC map generated from simulated data, Fig. 8(c) and (d), does not exhibit such an effect. The red curve in Fig. 8(b) is a low-pass filtered signal, obtained from a Fourier decomposition in z up to the fourth harmonic, and eliminates the strong high-frequency parasitic interference.

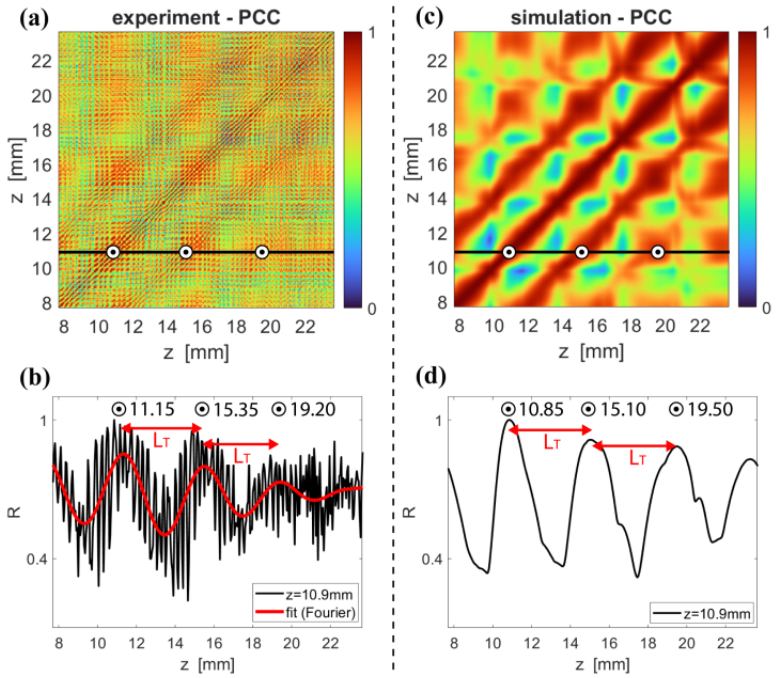

Fig. 8. PCC maps of the 1st order Fourier components of a double bifurcation grating. PCC maps generated from experimental (a) and simulated (c) data. (b) and (d): PCC cross-section taken along the black line in (a) and (c), respectively. The black circles mark the maxima of the black PCC cross-section lines and yield the fundamental Talbot length L_T (red arrows).

Both PCC maps show that the self-imaging contrast washes out with increasing distance more quickly than in the case of a single-bifurcation grating, see Fig. 5(a). This is attributed to the larger change of the carrier frequency around the vortex with increasing TC, i.e., the Talbot planes corresponding to the upper and lower half of the fork grating separate increasingly with increasing distance. The white circles mark the maxima of the black PCC cross-section lines and yield the fundamental Talbot length L_T (red arrows) to be 4.20 mm and 3.85 mm for the experiment and 4.25 mm and 4.40 mm for the simulation, respectively.

Fourier transform phase retrieval was applied to the positive 1st order shown in Fig. 7(c) and Fig. 7(f). In the experiment, the recovered phase shows two bifurcations separated by roughly 40 pixel along the grating lines, Fig. 9(a). This displacement is attributed to experimental artefacts like inhomogeneous illumination of the DOE and a slight tilt. However, other experimental conditions, in particular the parasitic interference, made the self-images of the 2nd Talbot distance the best candidate for phase retrieval, and in fact, the recovered phase shows a double-bifurcation. The simulation, Fig. 9(c) shows an ideal double-bifurcation in the center. For better visualization of the phase vortices, the carrier frequency was subtracted in Fig. 9(b) and Fig. 9(d). These images show that the beam carries OAM of $|l| = 2$. The black arrows highlight the phase change in one turn.

Optics EXPRESS

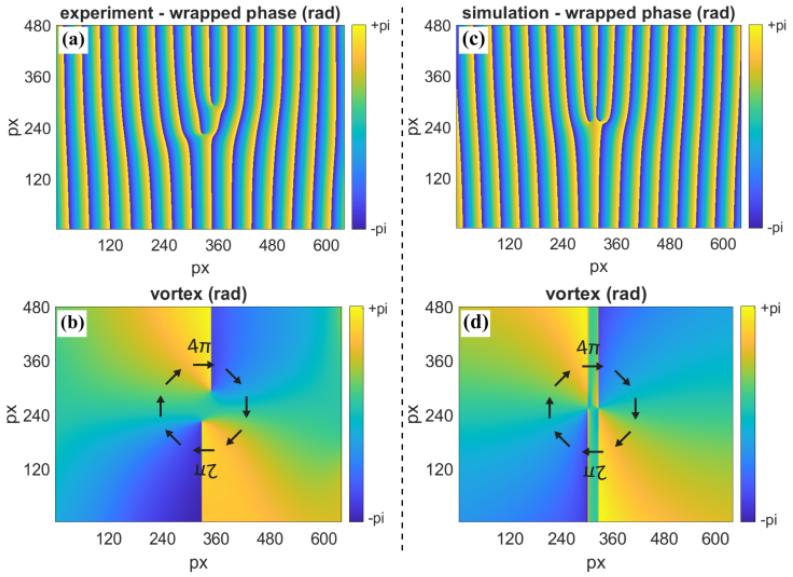

Fig. 9. Wrapped phase maps from the experiment (a) and simulation (c) and the corresponding demodulated helical phase in (b) and (d), respectively. The black arrows highlight the phase change in the azimuthal direction around the singularities.

4.3. *Far-field measurement*

To complete the assessment of the double-bifurcation fork grating, a measurement of its far-field diffraction pattern was performed. Figure 10(a) sketches the experimental setup. Figure 10(b) shows the characteristic intensity profile of the diffracted beam orders depending on their TC. The black arrows of the $\pm 1^{st}$ orders indicate the transversal projection of the $\boldsymbol{k}$-vector on the x-y-plane, together with the circumferential phase information which continuously runs from 0 to 4π in one roundtrip for $|l| = 2$. As demonstrated by Alperin et al. [42], passing a vortex beam through a cylindrical lens (CL) leads to an interference pattern at the lens focal plane as sketched in Fig. 10(c). The inclination of the focal line with respect to the y-axis is given by the magnitude of the transverse component k_x of the wave vector $\boldsymbol{k}$. Meanwhile, the y-component remains unaltered. The phase is uniform for $|l| = 0$ in the zero diffraction order. However, destructive interference due to the horizontal phase components leads to the minima of the focal lines displaced in x-direction. The number of these dark fringes corresponds to the TC, while the inclination of the line encodes its sign.

Figure 10(d-f) show the beam profile of the -1^{st}, 0^{th} and $+1^{st}$ diffraction order measured using a plano-convex lens to reduce their size. They correspond to the expected shapes from Fig. 10(b). Note that all intensity profiles show some inhomogeneity, caused by the non-Gaussian beam shape and the non-uniform camera sensitivity. Further, the diaphragm shutter and sample holder added some ring-shaped diffraction patterns. Nevertheless, the results are significant because the high-intensity rings of the $\pm 1^{st}$ diffraction orders are clearly seen, while there is no distinct ring structure for the 0^{th} diffraction order. Figure 10(g-i) depict the measurement results in the focal plane of a 3D-printed cylindrical lens with a focal length of 120 mm. The white dashed lines highlight the minima. Again, the results correspond to the expected shapes from Fig. 10(c). These far-field results demonstrate that the fork grating with a double-bifurcation performs as expected.

Optics EXPRESS

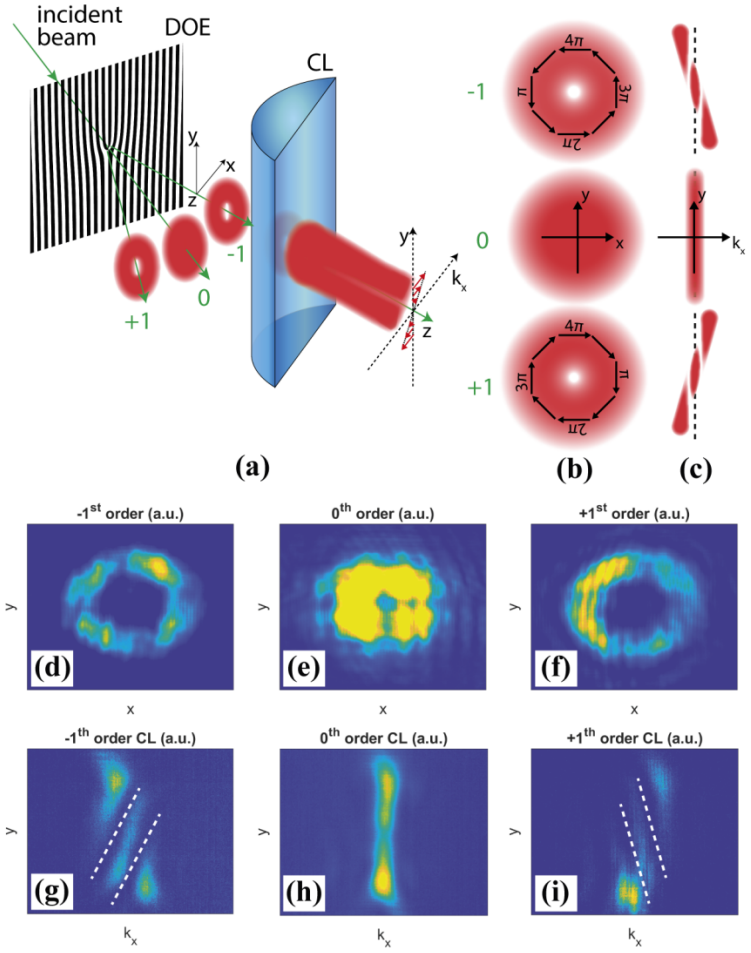

Fig. 10. (a) Far-field measurement set-up and effect of a cylindrical lens (CL) on the diffracted beams of a double-bifurcation fork grating. (b) Beam profiles of the -1st, 0th, + 1st diffraction orders (green numbers) carrying a TC of l = -2, l = 0, l = + 2, respectively. (c) Corresponding intensity patterns at the focal plane of the CL. (d-f) Far-field camera images of the -1st, 0th, + 1st diffraction orders. (g-i) Interference pattern in the focal plane of the CL. Dark fringes are marked by white dashed lines.

5. Conclusions

In this work, we introduced a method to determine OAM including the TC in the near-field of fork gratings using the Talbot effect. In doing so, the self-imaging of binary fork gratings was demonstrated in the THz regime, and the fundamental Talbot length was experimentally determined and compared to simulations. The far-field diffraction orders of fork gratings are known to carry TC. However, the far-field diffraction pattern of a DOE is identical to the Fourier transform of the scattering plane. Based on the Talbot effect the TCs generated by single and double bifurcation fork gratings were evidenced experimentally and with appropriate simulations in the near-field. Finally, to confirm the findings from the near-field, measurements of its far-field diffraction were performed. The TC was measured by means of a 3D-printed cylindrical lens. This showed good agreement with research done in other regimes of the electromagnetic spectrum.

Optics EXPRESS

The proposed method is not limited to the THz regime, but can be applied to the entire electromagnetic spectrum provided the appropriate equipment for imaging is at disposal, and the fork grating parameters are scaled to the wavelength. The ability to recover the helical phase from near-field diffraction closes a gap in the detection of TC in the nearfield of fork gratings. Because fork gratings are widely used to generate OAM carrying beams, our work will bring an additional impetus to the field of communication and imaging technology, e.g. by combining nano-printing and fiber technology to get a reliable TC read-out at the end of an information channel. To measure the TC of OAM beams in the near-field could also be decisive when there is no possibility for the beam to propagate to the far-field. A typical example for short propagation distances are photonic circuits or information technology in general. The applicability is also highlighted when considering diffractive optical elements that change their number of bifurcations dynamically, and its topological charges need to be known or verified.

Acknowledgements. The authors would like to thank Dr. Ivan Shorubalko, Empa, for his help in the fabrication of the DOEs. Further, we like to thank Dominic Zwyssig, Empa, for 3D printing the DOE holders and the cylindrical lens.

Disclosures. The authors declare no conflicts of interest.

Data availability. Data underlying the results presented in this paper are not publicly available at this time, but may be obtained from the authors upon reasonable request.

References

1. V. Y. Bazhenov, M. S. Soskin, and M. V. Vasnetsov, "Screw Dislocations in Light Wave-Fronts," J. Mod. Opt. **39**(5), 985–990 (1992).
2. L. Allen, M. W. Beijersbergen, R. J. C. Spreeuw, and J. P. Woerdman, "Orbital Angular-Momentum of Light and the Transformation of Laguerre-Gaussian Laser Modes," Phys. Rev. A **45**(11), 8185–8189 (1992).
3. Q. W. Zhan, "Cylindrical vector beams: from mathematical concepts to applications," Adv. Opt. Photonics **1**(1), 1–57 (2009).
4. N. Bozinovic, Y. Yue, Y. X. Ren, M. Tur, P. Kristensen, H. Huang, A. E. Willner, and S. Ramachandran, "Terabit-Scale Orbital Angular Momentum Mode Division Multiplexing in Fibers," Science **340**(6140), 1545–1548 (2013).
5. F. Tamburini, G. Anzolin, G. Umbriaco, A. Bianchini, and C. Barbieri, "Overcoming the Rayleigh criterion limit with optical vortices," Phys. Rev. Lett. **97**(16), 163903 (2006).
6. S. Syubaev, A. Zhizhchenko, A. Kuchmizhak, A. Porfirev, E. Pustovalov, O. Vitrik, Y. Kulchin, S. Khonina, and S. Kudryashov, "Direct laser printing of chiral plasmonic nanojets by vortex beams," Opt. Express **25**(9), 10214–10223 (2017).
7. R. A. B. Suarez, L. A. Ambrosio, A. A. R. Neves, M. Zamboni-Rached, and M. R. R. Gesualdi, "Experimental optical trapping with frozen waves," Opt. Lett. **45**(9), 2514–2517 (2020).
8. Z. Q. Wang, R. Malaney, and B. Burnett, "Satellite-To-Earth Quantum Key Distribution via Orbital Angular Momentum," Phys. Rev. Appl. **14**(6), 064031 (2020).
9. X. L. Cai, J. W. Wang, M. J. Strain, B. Johnson-Morris, J. B. Zhu, M. Sorel, J. L. O'Brien, M. G. Thompson, and S. T. Yu, "Integrated Compact Optical Vortex Beam Emitters," Science **338**(6105), 363–366 (2012).
10. J. H. Zhou, "OAM states generation/detection based on the multimode interference effect in a ring core fiber," Opt. Express **23**(8), 10247–10258 (2015).
11. S. N. Khonina, V. V. Podlipnov, S. V. Karpeev, A. V. Ustinov, S. G. Volotovsky, and S. V. Ganchevskaya, "Spectral control of the orbital angular momentum of a laser beam based on 3D properties of spiral phase plates fabricated for an infrared wavelength," Opt. Express **28**(12), 18407–18417 (2020).
12. V. V. Kotlyar, A. A. Almazov, S. N. Khonina, V. A. Soifer, H. Elfstrom, and J. Turunen, "Generation of phase singularity through diffracting a plane or Gaussian beam by a spiral phase plate," J. Opt. Soc. Am. A **22**(5), 849–861 (2005).
13. L. L. Huang, X. Song, B. Reineke, T. Y. Li, X. W. Li, J. Liu, S. Zhang, Y. T. Wang, and T. Zentgref, "Volumetric Generation of Optical Vortices with Metasurfaces," ACS Photonics **4**(2), 338–346 (2017).
14. G. B. Wu, K. F. Chan, and C. H. Chan, "3-D Printed Terahertz Lens to Generate Higher Order Bessel Beams Carrying OAM," IEEE Trans. Antennas Propagat. **69**(6), 3399–3408 (2021).
15. N. Matsumoto, T. Ando, T. Inoue, Y. Ohtake, N. Fukuchi, and T. Hara, "Generation of high-quality higher-order Laguerre-Gaussian beams using liquid-crystal-on-silicon spatial light modulators," J. Opt. Soc. Am. A **25**(7), 1642–1651 (2008).
16. Y. M. Li, J. Kim, and M. J. Escuti, "Orbital angular momentum generation and mode transformation with high efficiency using forked polarization gratings," Appl. Opt. **51**(34), 8236–8245 (2012).
17. H. Guerboukha, K. Nallappan, and M. Skorobogatiy, "Toward real-time terahertz imaging," Adv. Opt. Photonics **10**(4), 843–938 (2018).
18. C. M. Liu, J. S. Liu, L. T. Niu, X. L. Wei, K. J. Wang, and Z. G. Yang, "Terahertz circular Airy vortex beams," Sci. Rep. **7**(1), 3891 (2017).

Optics EXPRESS

19. R. C. Keitel, B. le Feber, K. M. Dettlaff, R. Brechbuhler, E. De Leo, H. Rojo, and D. J. Norris, "Single-Pulse Measurement of Orbital Angular Momentum Generated by Microring Lasers," ACS Nano **15**(12), 19185–19193 (2021).
20. M. Malik, S. Murugkar, J. Leach, and R.W. Boyd, "Measurement of the orbital-angular-momentum spectrum of fields with partial angular coherence using double-angular-slit interference," Phys. Rev. A **86**(6), 063806 (2012).
21. G. Kulkarni, R. Sahu, O. S. Magana-Loaiza, R. W. Boyd, and A. K. Jha, "Single-shot measurement of the orbital-angular-momentum spectrum of light," Nat. Commun. **8**(1), 1054 (2017).
22. D. Z. Wei, Y. M. Wang, D. M. Liu, Y. Z. Zhu, W. H. Zhong, X. Y. Fang, Y. Zhang, and M. Xiao, "Simple and Nondestructive On-Chip Detection of Optical Orbital Angular Momentum through a Single Plasmonic Nanohole," ACS Photonics **4**(4), 996–1002 (2017).
23. J. M. Andersen, S. N. Alperin, A. A. Voitiv, W. G. Holtzmann, J. T. Gopinath, and M. E. Siemens, "Characterizing vortex beams from a spatial light modulator with collinear phase-shifting holography," Appl. Opt. **58**(2), 404–409 (2019).
24. S.Y. Fu, Y.W. Zhai, J.Q. Zhang, X.T. Liu, R. Song, H. Zhou, and C.Q. Gao, "Universal orbital angular momentum spectrum analyzer for beams," Photonix **1**(1), 19 (2020).
25. S. Buathong, S. Srisuphaphon, and S. Deachapunya, "Probing vortex beams based on Talbot effect with two overlapping gratings," J. Opt. **24**(2), 025602 (2022).
26. H. F. Talbot, "Facts Relating to Optical Science," Philos. Mag. **9**(56), 401–407 (1836).
27. B. Brezger, L. Hackermuller, S. Uttenthaler, J. Petschinka, M. Arndt, and A. Zeilinger, "Matter-wave interferometer for large molecules," Phys. Rev. Lett. **88**(10), 100404 (2002).
28. P. Hollmer, J. S. Bernier, C. Kollath, C. Baals, B. Santra, and H. Ott, "Talbot effect in the presence of interactions," Phys. Rev. A **100**(6), 063613 (2019).
29. M. Seifert, V. Ludwig, S. Kaeppler, F. Horn, P. Meyer, G. Pelzer, J. Rieger, D. Sand, T. Michel, J. Mohr, C. Riess, and G. Anton, "Talbot-Lau x-ray phase-contrast setup for fast scanning of large samples," Sci. Rep. **9**(1), 4199 (2019).
30. Z. G. Deng, N. Shapira, R. Remez, Y. Y. Li, and A. Arie, "Talbot effect in waveforms containing subwavelength multilobe superoscillations," Opt. Lett. **45**(9), 2538–2541 (2020).
31. J.H. Zhou, J.J. Wu, and H.Q. Pu, "Ring-shaped Talbot effect," Phys. Rev. A **103**(5), 053506 (2021).
32. P. Samadian and T. Hall, "Cylindrical Talbot effect for ultra-compact multimode interference couplers," Opt. Lett. **41**(17), 4110–4113 (2016).
33. S. Rasouli, A. M. Khazaei, and D. Hebri, "Talbot carpet at the transverse plane produced in the diffraction of plane wave from amplitude radial gratings," J. Opt. Soc. Am. A **35**(1), 55–64 (2018).
34. K. M. Dettlaff, E. Mavrona, P. Zolliker, and E. Hack, "Retrieving the Talbot length of arbitrary 2D gratings," Opt. Lett. **47**(7), 1814–1817 (2022).
35. Y. Hua, J. Y. Suh, W. Zhou, M. D. Huntington, and T. W. Odom, "Talbot effect beyond the paraxial limit at optical frequencies," Opt. Express **20**(13), 14284–14291 (2012).
36. M. S. Kim, T. Scharf, C. Menzel, C. Rockstuhl, and H. P. Herzig, "Talbot images of wavelength-scale amplitude gratings," Opt. Express **20**(5), 4903–4920 (2012).
37. J.W. Goodman, *Introduction to Fourier optics*. (W.H. Freeman, Macmillan Learning, New York, 2017), Fourth edition. ed.
38. L. Janicijevic and S. Topuzoski, "Fresnel and Fraunhofer diffraction of a Gaussian laser beam by fork-shaped gratings," J. Opt. Soc. Am. A **25**(11), 2659–2669 (2008).
39. W. B. Case, M. Tomandl, S. Deachapunya, and M. Arndt, "Realization of optical carpets in the Talbot and Talbot-Lau configurations," Opt. Express **17**(23), 20966–20974 (2009).
40. P.K. Rastogi and E. Hack, eds., *Phase estimation in optical interferometry*. (CRC Press, Boca Raton, 2015).
41. E. Mavrona, J. Graf, E. Hack, and P. Zolliker, "Optimized 3D printing of THz waveguides with cyclic olefin copolymer," Opt. Mater. Express **11**(8), 2495–2504 (2021).
42. S. N. Alperin, R. D. Niederriter, J. T. Gopinath, and M. E. Siemens, "Quantitative measurement of the orbital angular momentum of light with a single, stationary lens," Opt. Lett. **41**(21), 5019–5022 (2016).